# Optimal dome design for 700 bar hydrogen tank type IV : Hyperelliptic functions and shape factor

Abbas Tcharkhtchi, Stéphane Villalonga, Nader Zirak, Albert Lucas, Sedigheh Farzaneh, Mohammadali Shirinbayan

MERCK

# 2023 Merck Research Grant

# Green Hydrogen

**Sponsored by Group Coprorate Sustainability and Science & Technology Office**

Science and technology are at the heart of everything we do, driving innovations that enable us to contribute to a sustainable future. **In this endeavor, we are seeking for research proposals in the field of Green Hydrogen.**

Progress is currently made in green hydrogen production, e.g.:

- innovative electrolysis technologies
- system and industrial integration of hydrogen technologies, e.g., storage, distribution and application areas
- fuel cell development

Submitted proposals should include a proof of concept (Technology Readiness Level 3) and describe the innovativeness of the proposal as well as the impact on the future implementation of green hydrogen supply to the chemical and pharmaceutical industry.

**The best proposal will be awarded with one grant up to 200K € for one year with potential further collaboration**

**Apply now** to become part of our green hydrogen journey!

Researchgrants.merckgroup.com

*Merck is a leading science and technology company, operates across life science, healthcare and electronics. More than 60,000 employees work to make a positive difference to millions of people's lives every day by creating more joyful and sustainable ways to live.*

Received: 22 December 2022 | Revised: 17 February 2023 | Accepted: 23 February 2023

DOI: 10.1002/est2.469

RESEARCH ARTICLE

ENERGY STORAGE WILEY

# Optimal dome design for 700 bar hydrogen tank type IV: Hyperelliptic functions and shape factor

**Abbas Tcharkhtchi**[1] | **Stéphane Villalonga**[2] | **Nader Zirak**[1] | **Albert Lucas**[1] | **Sedigheh Farzaneh**[3] | **Mohammadali Shirinbayan**[1]

[1]Arts et Métiers Institute of Technology, CNRS, CNAM, PIMM, HESAM University, Paris, France

[2]CEA, DAM, Monts, France

[3]P4TECH, Boissy-Saint-Leger, France

**Correspondence**
Abbas Tcharkhtchi, Arts et Métiers Institute of Technology, CNRS, CNAM, PIMM, HESAM University, 75013 Paris, France.
Email: abbas.tcharkhtchi@ensam.eu

**Abstract**

The design of 700-bar composite tanks considering the safety factor imposes resistance to a bursting pressure greater than 1645 bars remains difficult which leads to the addition of carbon fibers. On the other hand, the specifications in terms of mass storage capacity and cost require the quantity of this same fiber to be limited. Thus, the optimal sizing of the composite remains one of the major challenges in the development of 700-bar tanks. This study is focused on an optimum design of dome contours for 700 bar hydrogen tank type IV considering the geometrical limitations, winding condition, and the feasible direction. The study is centered on the composite part and is separated into two parts: a study of the manufacturing process (filament winding) in its fundamental aspects and a structural calculation under HyperWorks to check the mechanical strength of the composite layers and optimize their stacking and the number to ensure the holding while minimizing the mass and therefore the cost of the tank.

**KEYWORDS**

filament winding, fuel storage, hydrogen storage vessel, numerical analysis, type IV vessel

## 1 | INTRODUCTION

Hydrogen is considered the energy sector of tomorrow. The hydrogen atom is very abundant on Earth in the form of water. Its molecule is the most energetic: 120 MJ/kg, that is, 2.5 times more than natural gas.[1] Hydrogen has an energy content of 39.4 kWh/kg while coal, depending on its form, oscillates in the range of 7.8 to 8.7 kWh/kg,[2] or about 5 times less per unit mass. It is neither polluting nor toxic and reactions With oxygen only generate water vapor. It is the lightest of the gases, which is a positive factor concerning safety (high speed of diffusion in the air). Besides a so-called "confined" situation (imprisoned with air in a closed volume), considering the different characteristics such as fuel toxicity, combustion products toxicity, flammable temperature, explosion energy, and flame emissivity it can be said that hydrogen shows more fuel combustion safety compared with natural gas.[3,4] It's transport and storage (under pressure or liquid) are possible. Fuel cells, which use hydrogen, are the most efficient means of directly converting chemical energy into electrical energy.[4-7] The development of hydrogen is driven by three elements[8-10]:

- $CO_2$: whatever the hypotheses that we can adopt on the level of fossil fuel reserves, the most urgent problem is to do everything possible to reduce greenhouse gas emissions, and in particular the $CO_2$,
- Energy independence: many countries are showing their desire to reduce their energy dependence by diversifying their energy sources and consequently by using hydrogen and thus improving their geopolitical situation.
- The inevitable depletion of fossil resources is expected toward the end of this century and we want to keep them as raw materials (plastics, etc) rather than burn them.

The main applications are oriented toward the generation of power for both industrial and residential, especially for mobile and portable technologies and transport. The major challenge presented by the use of hydrogen is storage and particularly in transport where the challenge is mass/price/resistance optimization.[11] This is why this energy source is currently an essential subject of study. Much work has been done and is in progress.[12]

To date, three types of hydrogen storage on board a vehicle can be envisaged[13,14]:

- Cryogenic storage in liquid form at 20 K (−253°C) under 10 bars (1 MPa) makes it possible to achieve interesting volume and mass densities but requires tanks with extensive thermal insulation to minimize evaporation.
- Storage on substrates in absorbed form, in particular on metal hydrides, has a very attractive volume density but a very low mass density. In addition, the kinetics, the temperature, and the cycling pressure remain, among other things, points that are difficult to control.
- The storage of hyperbaric gas in compressed form (currently 350 bars, or 35 MPa), finally, makes it possible to achieve a satisfactory mass density with composite tanks. The storage volume density remains low: a pressure of 700 bars (70 MPa) is inevitable to make this technology competitive.

To improve the performance of hyperbaric hydrogen storage, the researchers mainly play on two fronts: more efficient structural and internal lining materials for the tanks and more economical implementation. Hyperbaric tanks are classified into four categories.[15] The "type I" are completely metallic and the "type II" is metallic with binding (in principle in fiberglass) on their cylindrical part.[16] The "type III" are made of composite materials (initially in fiberglass and, increasingly, in carbon fibers) whose liner is metallic (initially in aluminum, recently in steel).[17] "Type IV" are composite tanks (mainly made of carbon fibers) whose liner is made of polymer (mainly thermoplastic of the polyethylene or polyamide type).[18] Figure 1 shows the different types of hydrogen tanks.

Among the various hydrogen storage methods, the CEA is particularly studying gaseous storage under pressure. The studies mainly concern composite and polymer reservoirs. This type of tank avoids the problems of wear and weight encountered on metal tanks, which makes them difficult to integrate into a vehicle. In this study, the principles of product design are to define the parameters that will use in the modeling of the reservoir. Such that, time and finally the design of the model itself and what is attached to it. The main objective of the project will be to determine the optimum profile of the dome of the liner of a tank by ensuring that:

- The winding process is industrial (no fiber slippage),
- The fiber is used to the best of its abilities (make the fiber work as much as possible in its longitudinal axis).
- The tank achieves the performance required by the application,
- The cost is minimal (and also the mass in the case of an embedded application).

A first theoretical approach to the mechanics of the fiber according to the profile (geodesic or not: CLAIRAUT curves), on the determination of an optimal profile can be approached. Depending on the results, the study of the wind and then the calculation of the behavior under the load of the tank will make it possible to check the choices made. The calculation application on a real object will enhance this study. Finally, the theory related to the filament winding process in the rest of this study to determine the parameters of the tank and the winding

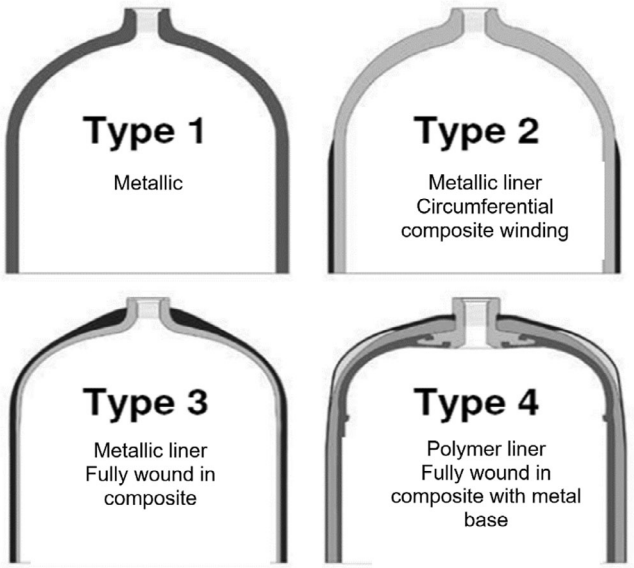


FIGURE 1 Different types of hydrogen tanks.

for the modeling of the winding and the construction of the model was developed.

## 2 | ANALYTICAL APPROACH

### 2.1 | Geodesy path

In filament winding, the fiber must follow a geodesic trajectory. Indeed this type of trajectory avoids the lateral sliding of the fiber. It is therefore not subjected to shear stresses which would be harmful because its properties are extremely weak in the transverse direction. Clairaut demonstrated a relationship between the radius of a surface and angle of geodesic line that can be drawn on it which was used in numerical application of this study. The following proof is based on references.[19,20] A geodesic line on a surface $S$ any curve $\Gamma$ inscribed on $S$ such that, at any point of $\Gamma$, $\Gamma$, $\vec{n} = \vec{N}$, either the normal to the surface coincides with the normal to the curve (Figure 2).

A curve drawn on a surface $S$ is described by the vector depending on $\theta$ and $\varphi$. Let $M$ be a point of the surface defined such that: $\vec{OM}\begin{pmatrix} x(\theta,\varphi) \\ y(\theta,\varphi) \\ z(\theta,\varphi) \end{pmatrix}$.

The length of a curve arc is defined by:

$$L = \int dS = \int \sqrt{dx^2 + dy^2 + dz^2}, \tag{1}$$

$$\begin{cases} dx = \dfrac{\partial x}{\partial \theta} \times d\theta + \dfrac{\partial x}{\partial \varphi} \times d\varphi \\ dy = \dfrac{\partial y}{\partial \theta} \times d\theta + \dfrac{\partial y}{\partial \varphi} \times d\varphi \\ dy = \dfrac{\partial z}{\partial \theta} \times d\theta + \dfrac{\partial z}{\partial \varphi} \times d\varphi \end{cases}. \tag{2}$$

By developing the expression (1) we obtain the first fundamental quadratic form:

$$L = \sqrt{\underbrace{\left(\left(\frac{\partial x}{\partial \theta}\right)^2 + \left(\frac{\partial y}{\partial \theta}\right)^2 + \left(\frac{\partial z}{\partial \theta}\right)^2\right) d\theta^2}_{G} + \underbrace{2 \times \left(\frac{\partial x}{\partial \theta}\frac{\partial x}{\partial \varphi} + \frac{\partial y}{\partial \theta}\frac{\partial y}{\partial \varphi} + \frac{\partial z}{\partial \theta}\frac{\partial z}{\partial \varphi}\right) d\theta \cdot d\varphi}_{F} + \underbrace{\left(\left(\frac{\partial x}{\partial \varphi}\right)^2 + \left(\frac{\partial y}{\partial \varphi}\right)^2 + \left(\frac{\partial z}{\partial \varphi}\right)^2\right) d\varphi^2}_{E}}. \tag{3}$$

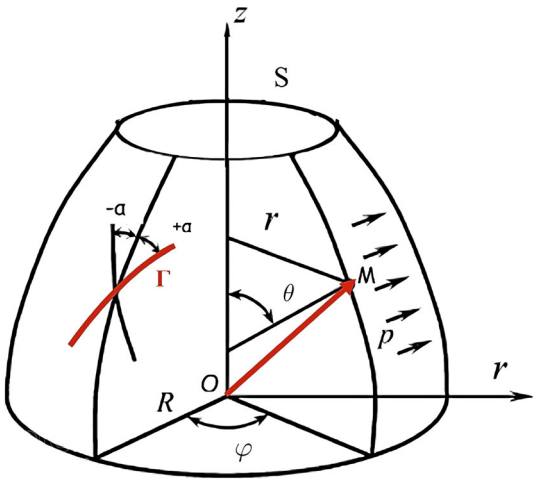


FIGURE 2 Surface parameterization.

We put:

$$\begin{cases} \phi' = \dfrac{\partial \phi}{\partial \theta} \\ \theta' = \dfrac{\partial \theta}{\partial \phi} \end{cases}.$$

Therefore can be obtained:

$$L = \int \sqrt{G + 2F\varphi' + E\varphi'^2} d\theta = \int \sqrt{G\theta'^2 + 2F\theta' + E} d\varphi. \tag{4}$$

Let $\Gamma$ be a curve drawn on a surface of revolution $S$. We define:

$$\vec{T} = \frac{d\vec{OM}}{ds},$$

the unit vector tangent to the curve (the fiber).

$$\vec{N} = \frac{\frac{d\vec{T}}{ds}}{\left\|\frac{d\vec{T}}{ds}\right\|}, \tag{5}$$

the unit vector normal to the curve.

Then $\left\|\frac{\partial \vec{OM}}{\partial \theta} \wedge \frac{\partial \vec{OM}}{\partial \phi}\right\| = EG - F^2$. We put $H^2 = EG - F^2$.

We also have $\vec{n} = \frac{\frac{\partial \vec{OM}}{\partial \theta} \wedge \frac{\partial \vec{OM}}{\partial \phi}}{H}$, the vector normal to the surface $S$.

The condition $\vec{n} = \vec{N}$ is equivalent at all points to the following system of differential equations:

$$\begin{cases} \frac{1}{2}\frac{\partial E}{\partial \theta}\left(\frac{d\theta}{ds}\right)^2 + E\frac{d^2\theta}{ds^2} + F\frac{d^2\varphi}{ds^2} + \left(\frac{\partial F}{\partial \varphi} - \frac{1}{2}\frac{\partial G}{\partial \theta}\right)\left(\frac{d\varphi}{ds}\right)^2 + \frac{\partial E}{\partial \theta}\frac{d\theta}{ds}\frac{d\varphi}{ds} = 0 \\ \left(\frac{\partial F}{\partial \theta} - \frac{1}{2}\frac{\partial E}{\partial \varphi}\right)\left(\frac{d\theta}{ds}\right)^2 + F\frac{d^2\theta}{ds^2} + G\frac{d^2\varphi}{ds^2} + \frac{1}{2}\frac{\partial G}{\partial \varphi}\left(\frac{d\varphi}{ds}\right)^2 + \frac{\partial G}{\partial \theta}\frac{d\theta}{ds}\frac{d\varphi}{ds} = 0 \end{cases} \tag{6}$$

Considering a surface of revolution parameterized according to Figure 3.

The $t$ is the parameter of the parametrized arc Γ. The surface of revolution is described by:

$$\vec{OM}\begin{pmatrix} X = r(t)\cos\phi \\ Y = r(t)\sin\phi \\ Z = Z(t) \end{pmatrix}, \tag{7}$$

$\frac{\partial \vec{OM}}{\partial \phi}\begin{pmatrix} -r\sin\phi \\ r\cos\phi \\ 0 \end{pmatrix}$ and $\frac{\partial \vec{OM}}{\partial t}\begin{pmatrix} r'\cos\phi \\ r'\sin\phi \\ Z' \end{pmatrix}$.

That is,

$$E = r^2, F = 0, G = r'^2 + Z'^2. \tag{8}$$

The first quadratic form is written in the form:

$$ds^2 = \underbrace{r^2 d\varphi^2}_{ds_p{}^2} + \underbrace{\left(r'^2 + Z'^2\right)dt^2}_{ds_m{}^2}, \tag{9}$$

$$\tan\alpha = \pm\frac{ds_p}{ds_m} = \frac{r d\phi}{\sqrt{r'^2 + Z'^2}dt} \text{ and } \cos\alpha = \sqrt{r'^2 + Z'^2}\frac{dt}{ds}, \tag{10}$$

$$\sin\alpha = r\frac{d\phi}{ds}. \tag{11}$$

In the case of a surface of revolution, the system of differential equation (5) is simplified:

$$\begin{cases} E\frac{d^2\varphi}{ds^2} + \frac{dE}{dt}\frac{d\varphi}{ds}\frac{dt}{ds} = 0 \\ -\frac{1}{2}\frac{dE}{dt}\left(\frac{d\varphi}{ds}\right)^2 + G\frac{d^2t}{ds^2} + \frac{1}{2}\frac{dG}{dt}\left(\frac{dt}{ds}\right)^2 = 0 \end{cases}. \tag{12}$$

The first equation is integrated as follows:

$$E\frac{d^2\varphi}{ds^2} + \frac{dE}{ds}\frac{d\varphi}{ds} = 0 \Leftrightarrow \frac{d}{ds}\left(E\frac{d\varphi}{ds}\right) = 0 \Leftrightarrow E\frac{d\varphi}{ds} = C \tag{13}$$

where $C$ is a constant, or $E\frac{d\phi}{ds} = r^2\frac{\sin\alpha}{r} = r\sin\alpha$.

So from Clairaut relation, on a geodesic line, $r \sin \alpha$ is Clairaut's constant; where $\alpha$ is the winding angle, and $r$ is radius of dome at the point considered. When $r = r_0$, the wrap angle is $\pi/2$, so we deduce that $C = r_0$. Finally, the fundamental relationship that will be used to determine the winding angle used according to the radius where the fiber passes is as follows:

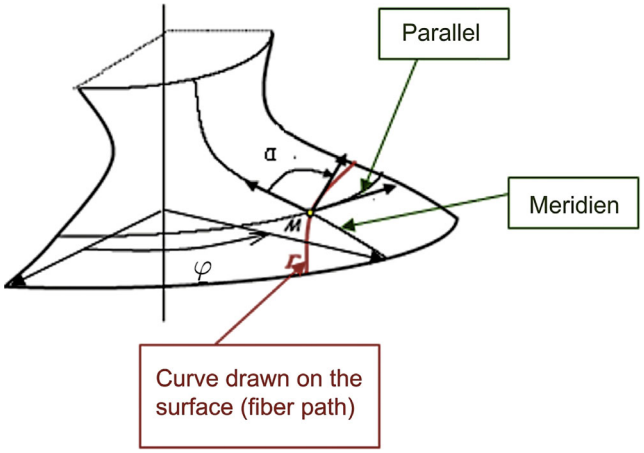


**FIGURE 3** The surface of revolution with different parameters.

$$r\sin\alpha = r_0. \tag{14}$$

## 2.2 | Semi-geodetic trajectories

The geodesic trajectories are able in the case of filament winding to define the windings which makes it possible to cover symmetrical surfaces of revolution. In our case, one end is open and the other is not. It is, therefore, not possible to cover the entire reservoir with such trajectories. The semi-geodesic trajectories use friction phenomenon of the fiber on surface to be able to deviate from the theoretical curve without there being any sliding of fiber.

The tension in the fiber $\vec{f}_t$ causes a force $\vec{f}_x = \frac{d\vec{f}_t}{ds}$ per unit area of the mandrel (liner) directed toward the center of curvature of the fiber. The resultant force can be divided into two components: the normal component $\vec{f}_n$ and the tangential component $\vec{f}_b$. The coefficient of friction of the fiber is:

$$\lambda = \frac{\left\|\vec{f}_b\right\|}{\left\|\vec{f}_n\right\|} = \frac{\vec{f}_z \cdot \vec{B}}{\vec{f}_z \cdot \vec{N}} = \frac{\vec{C} \cdot \vec{B}}{-\vec{C} \cdot \vec{N}}, \tag{15}$$

where $\vec{C}$ is the curvature vector $\vec{C} = \frac{d\vec{T}}{ds}$ and $\vec{B}$ the binormal vector $\vec{B} = \vec{T} \cdot \vec{N}$.

Substituting we get:

$$\lambda = \frac{A^2 r' \sin\alpha + A^3 r \frac{d\alpha}{ds}}{A^2 \sin^2\alpha - rr'' \cos^2\alpha} \Leftrightarrow \frac{d\alpha}{ds} = \frac{\lambda\left(A^2 \sin^2\alpha - rr'' \cos^2\alpha\right) - A^2 r' \sin\alpha}{A^3 r},$$

with $A = \sqrt{1 + r'^2}$.

We have $\cos\alpha = \frac{dS_m}{ds} = \frac{dZ}{ds}$ (see Figure 4), whence:

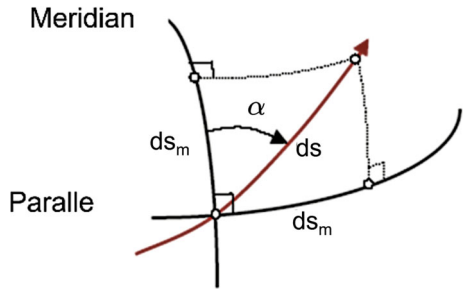


**FIGURE 4** The surface of revolution with different parameters.

$$\frac{d\alpha}{dZ} = \frac{\lambda\left(A^2 \sin^2\alpha - rr'' \cos^2\alpha\right) - r' A^2 \sin\alpha}{rA^2 \cos\alpha}. \tag{16}$$

Therefore, the end of dome angle $\alpha$ for the entire surface can be obtained by integrating this equation from $\alpha = 90°$. The thickness in axial direction, by assuming that values of the volume fraction of fibers and the number of fibers are constant in a strip section, is:

$$\begin{aligned} 2\pi rt \cdot \cos\alpha &= 2\pi r_c t_c \cos\alpha_c \\ t &= \frac{r_c \cos\alpha_c}{r\cos\alpha} t_c \end{aligned}. \tag{17}$$

where $r_c$ and $\alpha_c$ are the radius and wrap angle, respectively. Moreover, when the fiber is close to the base during winding, that is, $\alpha = 90°$, which means that t tends to infinity. The fibers accumulate in this area with each winding. To avoid this problem, the fiber can be wound at a different radius, greater than that of the base. Thus these trajectories use friction at bottom of the tank so that it is wound entirely. This allows us to remove metal bottom used so far to make the tank symmetrical and strengthen it, thus make a very significant weight gain.

## 2.3 | Dome equation

The stresses in a pressure vessel are related to the radius of curvature of the dome. To define the parameters geometry of the dome should be established. An element of a surface of revolution is delimited by two meridians and two parallels infinitely close to each other, as shown in Figure 5, where, $P$ represents external loading and $N$ is forces in tank per unit area and $R_m$, $R_p$, and $R_n$ are, respectively, the radii of curvature, at the considered point, of the meridian, of the parallel, and of the curve (the fiber). According to Refs. [21-23], in equilibrium condition, we have:

$$\Sigma F_\theta = 0 \Rightarrow \frac{\partial}{\partial\theta}\left(\rho N_\theta\right) + R_m \frac{\partial}{\partial\varphi}\left(N_{\varphi\theta}\right) - R_m \cos\theta + P_\theta \rho R_m = 0, \tag{18}$$

$$\begin{aligned} \Sigma F_\varphi &= 0 \\ &\Rightarrow \frac{\partial}{\partial\theta}\left(\rho N_{\theta\varphi}\right) + R_m \frac{\partial}{\partial\varphi}\left(N_\varphi\right) - R_m N_{\varphi\theta} \cos\theta + P_\varphi \rho R_m \\ &= 0, \end{aligned} \tag{19}$$

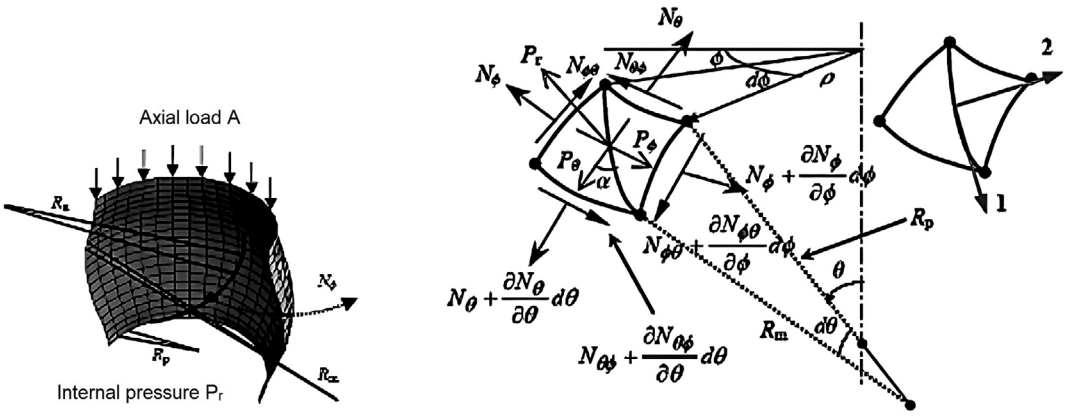


FIGURE 5 Loading an elementary surface of the tank.

$$\Sigma F_r = 0 \Rightarrow \frac{N_\theta}{R_m} + \frac{N_\varphi}{R_p} = P_r. \tag{20}$$

The pressure forces are normal to the surface so $P_\theta$ and $P_\varphi$ are zero. Moreover, the loading is symmetric by rotation therefore derivative of $N_\varphi$ compared with $\varphi$ is worthless. Thus Equation (4) also gives $N_{\theta\varphi} = 0$. According to the bibliographical references,[23-25] we also have:

$$R_m = -\frac{\left(1+z'^2\right)^{\frac{3}{2}}}{z''} \text{ and } R_p = -r\frac{\sqrt{1+z'^2}}{z'}.$$

We have:

$$Y = \frac{\rho}{\rho_0},\ k_a = \frac{A}{\pi P \rho_0^2},$$

$A$ is the external loading of the tank. In our case, $A = 0$. We have the following relation from[10]:

$$\frac{N_\varphi}{N_\theta} = \tan^2\alpha = 2\left(\frac{Y^2}{k_a + Y^2}\right) - \frac{R_p}{R_m} \tag{21}$$

That is:

$$\begin{aligned} \frac{N_\varphi}{N_\theta} &= 2 - \frac{R_p}{R_m} \\ \frac{rz''}{z'\left(1+z'^2\right)} &= 2 - \tan^2\alpha. \end{aligned} \tag{22}$$

And according to Clairaut's relation, we have:

$$\frac{rz''}{z'\left(1+z'^2\right)} = \frac{2r^2 - 3r_0^2}{r^2 - r_0^2}. \tag{23}$$

So the equation of the dome is:

$$z(r) = -\int \frac{r^3 dr}{\sqrt{(1-r^2)(r^2-a_1)(r^2-a_2)}} + C, \tag{24}$$

where:

$$\begin{aligned} a_1 &= \frac{1}{2}\left(\sqrt{\frac{1+4r_0^2}{1-r_0^2}} - 1\right) \\ a_2 &= -\frac{1}{2}\left(\sqrt{\frac{1+4r_0^2}{1-r_0^2}} + 1\right) \end{aligned}.$$

We determine the constant $C$ equal to $2.4 \times 10^{-3}$ thanks to the boundary conditions, namely that $z = 0$ when $r = R$. This will be the equation of the dome under pressure, that is, deformed because it is considered that the fiber will have to work longitudinally at maximum stress, that is, at maximum pressure. Moreover, during winding, the surface on which the fiber is deposited will be modified by the thickness of the previous layers.

## 2.4 | Simplified practical method of building the dome

In practice, to trace profile of the dome, an incremental method is used. Figure 6 shows the dome configuration.

We have:

$$\cos\psi = -\frac{r}{R_p}. \tag{25}$$

So according to the three previous equations:

$$R_m = \frac{r}{\cos\psi(2-\tan^2\alpha)}. \quad (26)$$

Finally:

$$\psi = \Sigma\Delta\psi$$
$$r = R - \Sigma\Delta r$$
$$X = \Sigma\Delta x$$

Also:

$$\Delta r = R_m \cdot \Delta\psi \cdot \sin\psi$$
$$\Delta x = R_m \cdot \Delta\psi \cdot \cos\psi$$

We start from $\begin{cases} r = R \\ \psi = 0 \\ \alpha = \sin^{-1}\left(\frac{r_0}{r}\right) \end{cases}$. *A* value of the increment $\Delta\Psi$ is fixed. We recalculate step by step for each increment *r*, *X*, and $\alpha$.

There is a point of inflection where $R_m$ is undefined, either for $\alpha = 54.7°$ or $r = 1.22 \times r_0$. In design, the outer radius of the base was chosen greater than the opening radius of the latter. Figure 7 indicates the Geodesic profiles of domes according to the external radius of the pass.

In the case of our study, the parameters are fixed:

- $r_0 = 34$ mm,
- $R = 114$ mm.

So, the profile of the dome model shown in Figure 8 is plotted in pink. If we superimpose on this an ellipsoidal dome profile with parameters $a = 57$ mm and $b = 37$ mm, we see that these two profiles are very close to each other. In the rest of this study, we will use the ellipse profile for reasons of simplicity. This profile will also be that of the base which must be continuous with the liner so as not to create additional stress concentration zones.

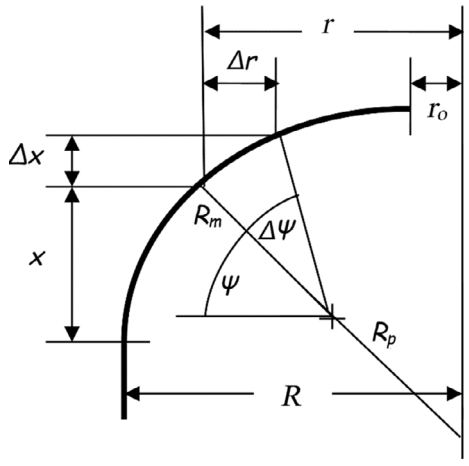


FIGURE 6 Dome configuration.

## 3 | MATHEMATICAL AND NUMERICAL ANALYSIS

### 3.1 | Netting analysis

Netting analysis is a method that makes it possible to determine the optimum winding angle of the tank according to the stresses to which it is subjected.[19,24,26] Considering that the reservoir is wound helically and circumferentially, the winding must be geodesic or semi-geodesic (Figure 9).

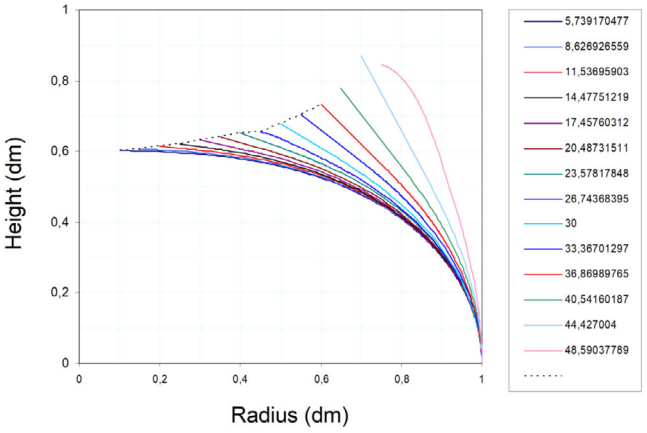


FIGURE 7 Geodesic profiles of domes according to the external radius of the pass.

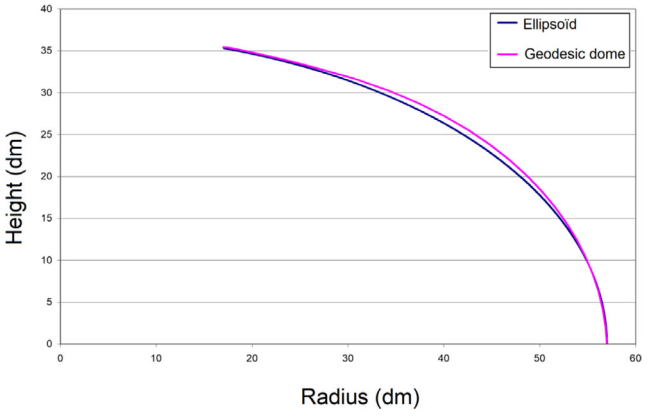


FIGURE 8 Comparison of dome profiles.

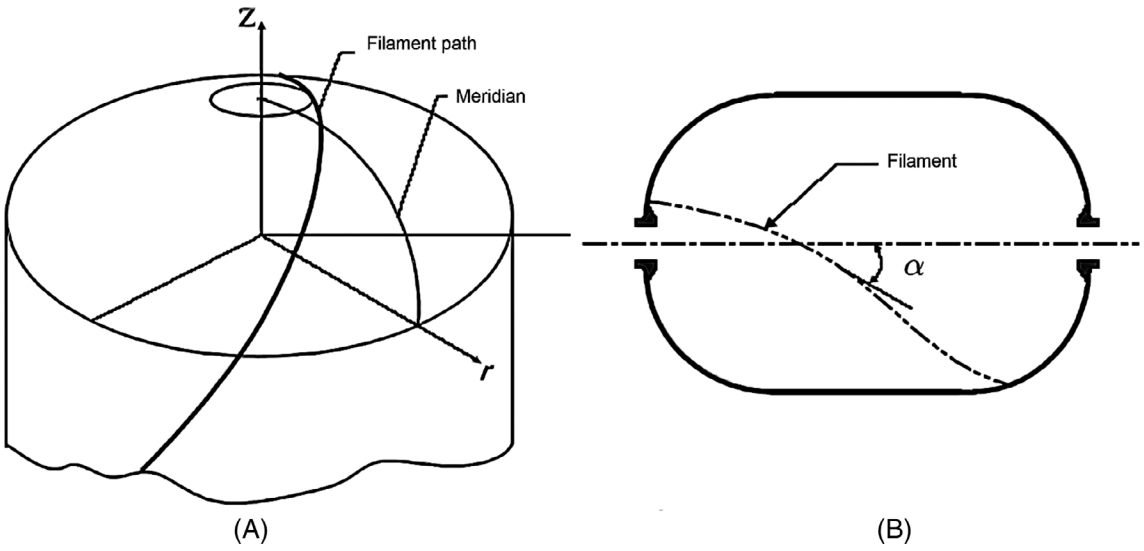


FIGURE 9 Schematic of Geodesic winding.

The development based on the theory of composites[27] leads to the result (Δ) of the appendix, which gives:

$$\left.\begin{aligned} N_\theta &= \sigma_1 \cos^2\alpha + \sigma_2 \sin^2\alpha - \tau_{12} \sin 2\alpha \\ N_\varphi &= \sigma_1 \sin^2\alpha + \sigma_2 \cos^2\alpha - \tau_{12} \sin 2\alpha \end{aligned}\right\}, \tag{27}$$

and

$$\left.\begin{aligned} \varepsilon_1 &= \varepsilon_\theta \cos^2\alpha + \varepsilon_\varphi \sin^2\alpha \\ \varepsilon_2 &= \varepsilon_\theta \sin^2\alpha + \varepsilon_\varphi \cos^2\alpha \\ \gamma_{12} &= (\varepsilon_\varphi - \varepsilon_\theta) \sin 2\alpha \end{aligned}\right\}. \tag{28}$$

Moreover, the generalized Hooke's law gives:

$$\begin{Bmatrix} \varepsilon_1 \\ \varepsilon_2 \\ \gamma_{12} \end{Bmatrix} = \begin{bmatrix} \frac{1}{E_1} & -\frac{\nu_{12}}{E_1} & 0 \\ -\frac{\nu_{21}}{E_2} & \frac{1}{E_2} & 0 \\ 0 & 0 & \frac{1}{G_{12}} \end{bmatrix} \begin{Bmatrix} \sigma_1 \\ \sigma_2 \\ \tau_{12} \end{Bmatrix}. \tag{29}$$

with $E_{1\nu_{12}} = E_{2\nu_{21}}$, where $\nu$ are the Poisson's ratios and $E$ Young's moduli in the two main directions.

Relations (28) gives:

$$\varepsilon_1 - \varepsilon_2 + \gamma_{12} \cot an\alpha = 0. \tag{30}$$

And (28) gives:

$$\frac{\sigma_1}{e_1} - \frac{\sigma_2}{e_2} + \frac{\tau_{12}}{G_{12}} \cot an 2\alpha = 0, \tag{31}$$

with $e_1 = \frac{E_1}{1+\nu_{12}}$, $e_2 = \frac{E_2}{1+\nu_{21}}$.

Then (26) and (30) lead:

$$\left.\begin{aligned} \sigma_1 &= \frac{1}{2c}\left[(N_\theta + N_\varphi)\left(1 + \frac{2G_{12}}{e_2}\tan^2 2\alpha\right) + \frac{N_\theta - N_\varphi}{\cos 2\alpha}\right] \\ \sigma_2 &= \frac{1}{2c}\left[(N_\theta + N_\varphi)\left(1 + \frac{2G_{12}}{e_1}\tan^2 2\alpha\right) - \frac{N_\theta - N_\varphi}{\cos 2\alpha}\right] \\ \tau_{12} &= \frac{G_{12}\tan 2\alpha}{c\cos 2\alpha}\left[N_\varphi\left(\frac{\sin^2\alpha}{e_1} + \frac{\cos^2\alpha}{e_2}\right) - N_\theta\left(\frac{\cos^2\alpha}{e_1} + \frac{\sin^2\alpha}{e_2}\right)\right] \end{aligned}\right\}, \tag{32}$$

with $c = 1 + G_{12}\left(\frac{1}{e_1} + \frac{1}{e_2}\right)\tan^2 2\alpha$.

In addition, properties of the fiber are used to maximum when stressed layers of a laminate are aligned with direction in which stress is maximum. This implies that stress is maximum in the direction of fiber and shear stress is zero which is $\varepsilon_\theta = \varepsilon_\Phi$ equivalent to:

$$\tau_{12} = 0 \Rightarrow \frac{N_\varphi}{N_\theta} = \frac{\sin^2\alpha + k_e \cos^2\alpha}{\cos^2\alpha + k_e \sin^2\alpha}, \tag{33}$$

where,

$$k_e = \frac{e_2}{e_1} = \frac{E_2(1+\nu_{12})}{E_1(1+\nu_{21})}. \tag{34}$$

In the case of a laminate and to simplify calculations, it is considered that the mechanical properties of matrix are negligible compared with those of fibers in stressed layers. This is the basic assumption of netting analysis. Thus, as $E_1 >> E_2$, $k_e = 0$ and:

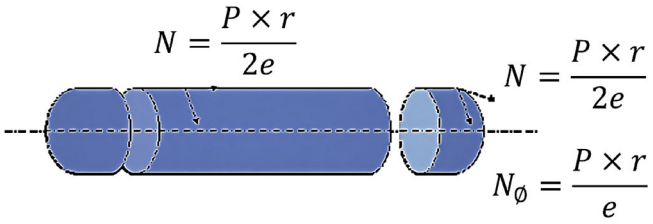


**FIGURE 10** The circumferential stress on a generatrix of the tube directed along its cross-section $N_{\phi}$.

$$\frac{N_{\varphi}}{N_{\theta}} = \tan^2\alpha. \tag{35}$$

The angle $\alpha$ is the wrap angle. Note that in a pressurized tube $P$ shown below, the circumferential stress on a generatrix of the tube directed along its cross-section $N_{\phi}$ is of the form (Figure 10):

$N_{\phi} = \frac{pR}{e} = 2N_{\theta}$, according to the thin tube theory,

with $N_{\theta}$ the stress along the axis of the tube, $R$ the radius of the tube, and $e$ the thickness of the tube. This case is the ideal case in which the maximum stress takes place in the direction of the fibers. The simplifying assumptions of this theory allow us to determine an ideal angle for which the maximum stress is in direction of the fibers, which $\frac{N_{\phi}}{N_{\theta}} = 2 = \tan^2\alpha$ give $\alpha = 54.7°$.

## 3.2 | Effect of composite layers thickness

The netting analysis leads to the evaluation of the thickness of the composite layers. We isolate an element of the winding, that is, a layer formed by two plies oriented at $\pm\alpha$, such that the section is unity. Let $N_{f\alpha}$ be the stress in a ply and $t_{f\alpha}$ the thickness of the layer. According to the static equilibrium equations, in projection on $e_{\theta}$, we have:

$$F_{\alpha} + F'_{\alpha} - N_{\theta}S = 0. \tag{36}$$

The action of the 90° bend along $e_{\theta}$ is not taken into account since the transverse properties of the fiber are negligible. $S$ is the section of the fold.

$$\frac{2N_{f\alpha}t_{f\alpha}1\cos^2\alpha}{2} - \frac{pR}{2} = 0, \tag{37}$$

where $t_{f\alpha} = \frac{pR}{2N_{f\alpha}\cos^2\alpha}$.

We project in the same way according to $e_{\Phi}$:

$$F_{\alpha} + F''_{\alpha} + F_{90} - N_{\varphi}S = 0, \tag{38}$$

$$\frac{2N_{f\alpha}t_{f\alpha}1\sin^2\alpha}{2} + N_{90}t_{f90}1 - \frac{pR}{2} = 0, \tag{39}$$

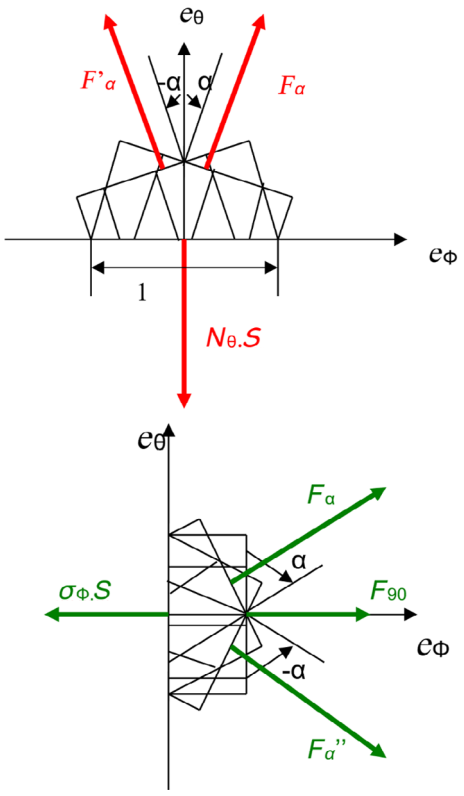


**FIGURE 11** Evaluation of the thickness of the composite layers.

$$t_{f90} = \frac{pR}{2N_{f90}}\left(2 - \tan^2\alpha\right). \tag{40}$$

For circumferential windings (Figure 11), it is advised[28] to divide the stress in the fiber by the factor $\left(1 + \frac{N_{f90}}{E_f}\right)$, where $E_f$ is the modulus of elasticity of the fiber. An iterative procedure makes it possible to obtain the result, for which the correction is quite weak.

## 3.3 | Effect of number of pleats

In the filament winding process, several ($N$) fiber coils can be used in parallel to form a winding strip of width $W$. Each coil has a cross-sectional area (CSA), the eigenvalues of which can be found to each fiber from $t_{fp} = \frac{N(\mathrm{CSA})}{W}$. The fiber thickness of a ply is defined by the expression.

Then the breaking stress of a fiber in a laminated composite is lower than that which can be found in a unidirectional ply. Thus, a coefficient of 70% to 80% will be applied to the values given by the fiber supplier. Added to this, the value of this stress is even lower in the case of the folds because there are interlacings of the folds and the area of discontinuity of the surface at the

level of the junction between the dome and cylinder which is a place of concentration of constraints. We have the following ratio $\frac{N_{\text{rupture}\alpha}}{N_{\text{rupture}90}}$ which is between 75% and 100%.

The wrap thickness is distributed between 90° and $W_\alpha$ is chosen so that the tank can be covered with an integer number of windings and without overlapping. $W_{90}$ is chosen so that the wrap angle is closest to the ideal 90°. $V_{f\alpha}$ and $V_{f90}$ are the fiber volume fractions, they depend on the process. According to Ref. [11], for carbon fiber, we have volume fractions of the order of 0.50 to 0.55 for the helical winding and 0.60 to 0.65 for the circumferential winding. We have:

$$t_{c\alpha} = \frac{N_\alpha(\text{CSA})}{W_{\theta\alpha} V_{f\alpha}}$$
$$t_{c90} = \frac{N_{90}(\text{CSA})}{W_{90} V_{f90}} \quad \text{and } t_{c\alpha} + t_{c90} = t_{\text{total}}.$$

In practice, correction coefficients will be assigned to these thicknesses (1.40 for the helical winding and 1.10 for the circumferential winding) which allow a margin to be taken. Thus we obtain the number of folds necessary.

### 3.4 | Geometry of tank

The values of breaking stress of fiber, radii of connectors, cylinder, and desired volume for the tank, angle of rolling $\alpha$, thicknesses of folds and their number, and dome profile were obtained in the previous sections. So, the values of volume of liner (volume of two domes added to volume of cylinder) and composite, mass of material (polymer and composites), and volume of the tank can be calculated.

We size the base whose upper surface in contact with the composite will be continuous with the liner (the equation is the same as the liner), which gives us its mass. This results in volumetric and gravimetric capacities which must be optimal for the minimum dimensions and mass of the reservoir. In the case of our study, the dimensions are imposed in the specifications for the system to be integrated into a vehicle. However, the parameters set may not allow the reservoir to be fully optimized. Indeed there is another ratio $R/r_0$ for which the size of the tank and the mass of fibers is minimal and thus the volumetric and gravimetric capacities are maximized.

Figure 12 shows the optimum in terms of mass and gravimetric and volume capacities are located at the level of the red dotted line, that is, for a diameter of ~150 mm, therefore, for a 2 L tank.

Furthermore, it should be noted that the profile optimized for winding process is not necessarily optimal

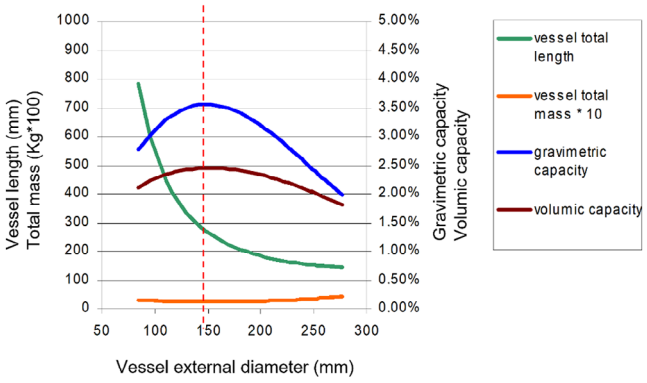


FIGURE 12 Tank type IV, 700 bar.

profile from a mechanical point of view. However, the process and permitted size impose characteristics of the tank.

## 4 | MODELING AND STUDY OF THE TANK

The various principles developed in first part of this report are used in the design and manufacturing process of tanks. The various design stages are as follows: the Cadwind tool is used to determine thicknesses of the tank, configuration of fibers, and types of winding to be carried out. From the Cadwind data, we build a CAD geometry that we use to perform the meshing and the finite element analysis, then the optimization of the structure and the geometry.

Cadwind is a filament winding simulation tool. It allows us to virtually manufacture the composite whose initial architecture is given by the netting analysis. Cadwind calculates a windable architecture with a detailed description of the angles of all the layers in particular at the level of the domes.

We want to make a 2 L tank, with a diameter of 114 mm and a single base, in order to reduce the mass, with an outer diameter of 34 mm opening. The software makes it possible to select domes geometries that make it possible to carry out geodesic trajectories, which we wish to apply to carbon fibers. It also makes it possible to select the construction of tanks with a single base. The result is simulation of winding, type of patterns made and all the parameters useful for manufacturing.

The tank is, therefore, virtually coiled as can be seen below (Figure 13):

The simulation generates a tank geometry, that is, the geometry of the mandrel, that is, the liner, and the configuration of the composite layers as well as the winding parameters. Text files can be used to create the geometry and the laminate as we will see later.

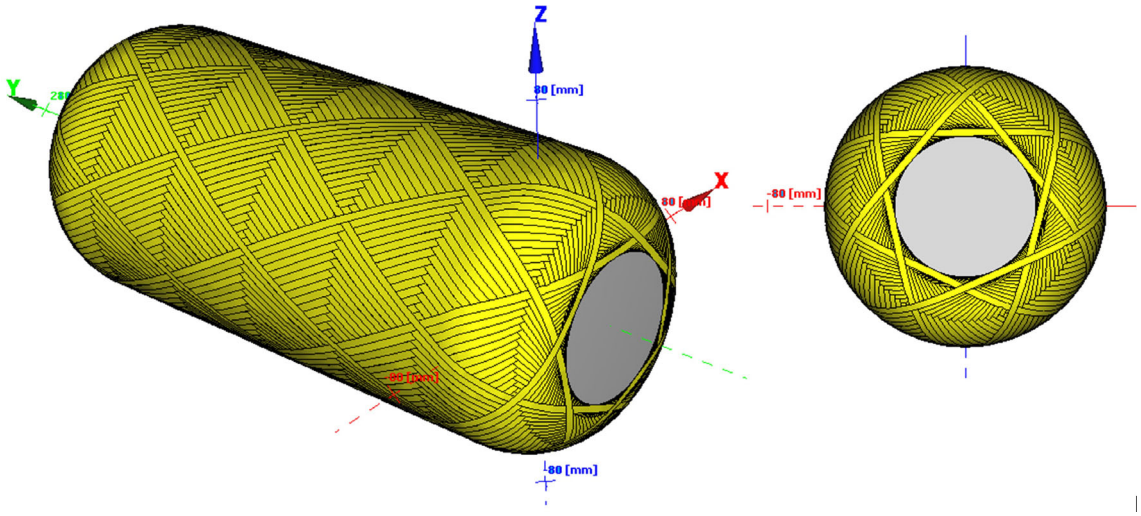


FIGURE 13 The tank coiled.

These files are those that interest us in order to carry out the modeling. Cadwind also provides all the mandrel rotation speed and displacement parameters for the carriage unwinding the fiber and the parameters used directly in the programming of the tank manufacturing process.

In the data exported from Cadwind, we extract files that define the laminates according to $r$ and $z$ as well as the initial geometry of the mandrel, that is to say the liner. We enter the profile of the dome point by point in the Catia sketch, which we smooth. In addition, the base is defined using a Cosmosworks module. The composite winding is represented by a shell corresponding to the outer surface of the liner and base assembly as can be seen in the images on the following page. The CAD files will be imported into the finite element software to serve as support for the mesh (Figure 14).

HyperMesh is a meshing tool of Hyperworks suite, a tool acquired by ENSAM for this project. Modeling of the tank has two main objectives: to tend toward an optimization of the geometry of this one in order to minimize the mass by allowing respect of specifications in terms of mechanical resistance and to demonstrate the feasibility of this modeling under HyperMesh (then the processing in static study of this model under OptiStruct), and thus to validate the acquisition of software by the laboratory for applications to composites in particular.

In the first step, the geometry from Catia files was imported. The properties of materials including aluminum, liner which was in polymer, and composite, are in Table 1. The loads, namely embedding of base as well as the pressure of 1645 bars in the tank. As can be seen in the first part, properties of carbon fibers are different in the case of circumferential and helical winding (supplier data), so we define two materials for the layers of different natures.

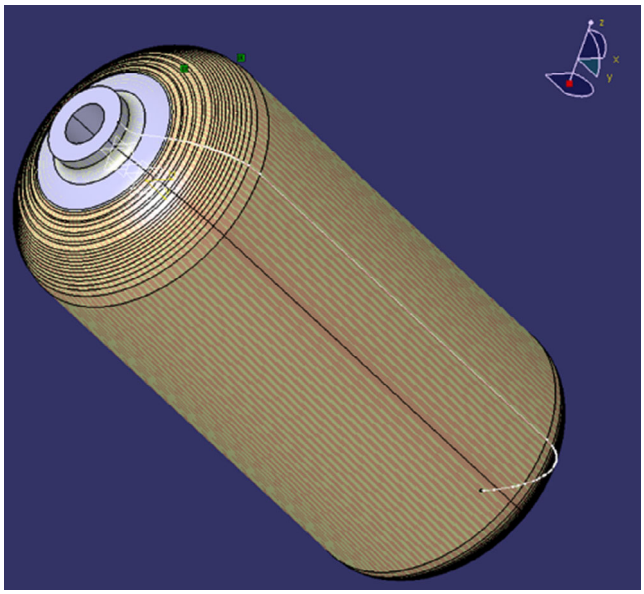

FIGURE 14 Cad design of the tank.

The essential part of the modeling is definition of properties of composite winding. In reality, the composite layer is made up of intersecting fibers and we get a kind of woven texture. Each pattern corresponds to a specific laminate.

However, for practical reasons it is not possible to model all the patterns of each layer (of which there are ∼30). To model the winding, we will discretize the surface of the reservoir into crowns, to which we assign a particular laminate. Indeed, in the realization of the winding there are two aspects which lead to the presence of different angles according to the radius and the layer

**TABLE 1** Material properties.

| Material | $E_1$ ($\times 10^3$) MPa | $E_2$ ($\times 10^3$) MPa | $\nu_{12}$ | $G_{12}$ ($\times 10^3$) MPa | $G_{23}$ ($\times 10^3$) MPa | $G_{13}$ ($\times 10^3$) MPa | $\rho$ (g/cm$^3$) |
|---|---|---|---|---|---|---|---|
| Helical composite layers | 140 | 10 | 0.26 | 4.8 | 3.2 | 4.8 | 1.57 |
| Circumferential composite layers | 151 | 10 | 0.26 | 5.3 | 3.3 | 5.3 | 1.6 |
| Aluminum | 75 | 75 | 0.3 | 29 | 29 | 29 | 2.8 |
| Polyamide 6 | 0.7 | 0.7 | 0.4 | 0.7 | 0.7 | 0.7 | 1.15 |

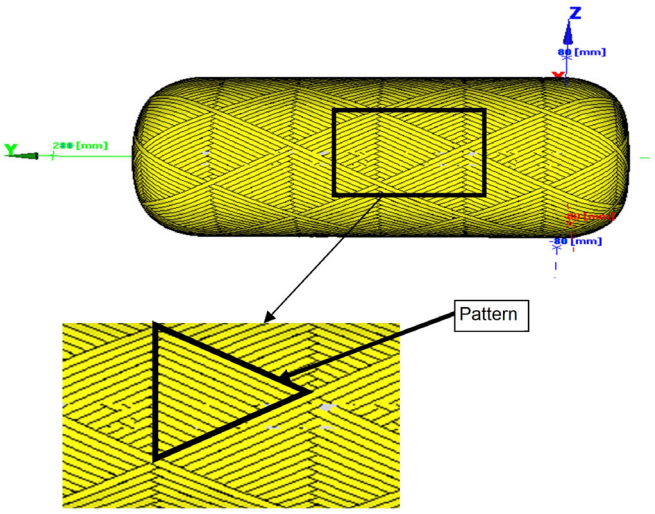


**FIGURE 15** The texture pattern of composite winding.

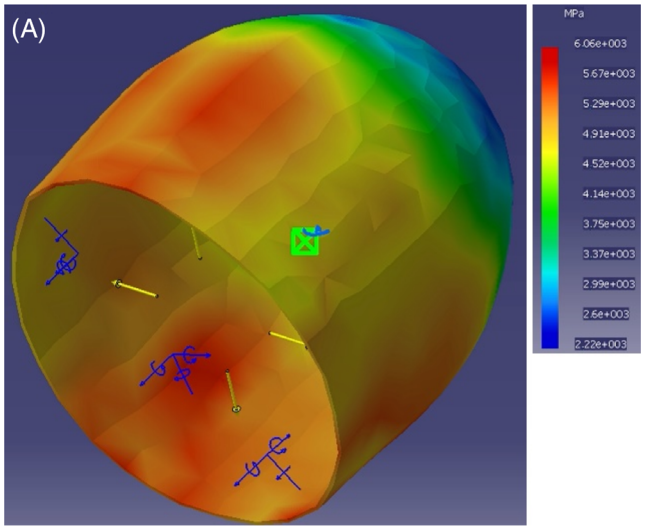


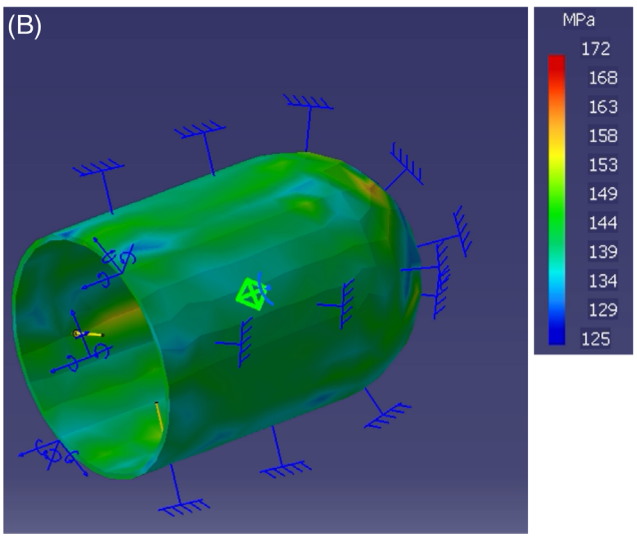


**FIGURE 16** von-Misses stress calculated for the tank: (A) without filament-wound composites and (B) treated winding consists.

where the fiber is located: on the one hand the change of angle is inherent to the manufacturing process as we saw it in the first part, with Clairaut's formula relating the wrap angle to the radius, on the other hand we superimpose several layers at different wrap angles in order to optimize the mechanical strength by minimizing the quantity fibers, because if the process gives us an angle that allows us to cover the tank, namely: $\sin \alpha = r_0/r$, that is, $\alpha = 17°$ in our study, layers are produced at other angles chosen arbitrarily to optimize The reservoir. In addition, the tank is asymmetrical because it has only one base, which gives the two domes different laminates. The treated winding consists of four layers at each of the following angles: 6°, 10°, 17°, 30°, 49°, and 70°, as well as a 90° layer on the cylindrical part of the tank at each change of angle, in order to ensure the resistance of the tank radially because in this zone, the fibers deposited helically are difficult to tension correctly. Thus the preparation work is quite tedious and in the context of the following projects, it would be interesting to set up a tool which would make it possible to create these files automatically, using a Visual Basic macro for example which would generate text files of type. Figure 15 shows the maximum von-Mises stress on the tank with respect to the different filament-wound composites conditions (Figure 16).

## 5 | CONCLUSIONS

In this study, a IV hydrogen storage tank under high pressure (700 bar) was investigated, in the sizing of the composite part of it, which gives the tank its mechanical characteristics and its resistance to pressure forces. The resistance of the tank depends on the filament winding of the fibers around the liner. According to the results, the calculation of the winding parameters derives from the differential geometry with regard to the trajectory of the fibers, and study of the stresses in fibers by application of principles of mechanics makes it possible to determine equations of the dome and that netting analysis brings up winding thicknesses and process limits.

The netting analysis which makes it possible to give the ideal helical winding angle for which stress is in direction of the fiber neglects the real stresses in each layer. Also a theoretical approach of a cylinder with a bottom effect whereas our case is a cylindrical reservoir has been applied. In addition, the theory of laminates is applied to the reservoir, whereas the strips of fibers are intersected at each winding and the pattern plays a determining role in the evaluation of the properties of the fiber (the breaking stress which is lower and the fiber is all the more weakened as the number of intersections is important). To have a model that is the most faithful to reality, it would be necessary to define each pattern as a stack in its own right with its own properties. However, these simplifications are necessary in order to obtain an easily usable model.

## NOMENCLATURE

### Abbreviations

| | |
|---|---|
| CSA | cross-sectional area |
| ENSAM | Ecole Nationale Supérieure d'Arts et Métiers |

### Symbols

| | |
|---|---|
| $L$ | length of a curve arc |
| $S$ | surface |
| $\vec{OM}$ | a point defined on the surface |
| $\vec{T}$ | a curve drawn on a surface |
| $\vec{N}$ | the unit vector tangent to the curve |
| $r$ | Clairaut's constant |
| $\sin\alpha$ | |
| $r$ | radius of dome at the point considered |
| $\vec{f}_t$ | tensile force |
| $\vec{C}$ | curvature vector |
| $\vec{B}$ | binormal vector |
| $r_c$ | radius angle |
| $\alpha_c$ | wrap angle |
| $A$ | external loading of the tank |
| $N_\Phi$ | meridional force |
| $N_\theta$ | circumferential force |
| $N_{\Phi\theta}$ | shear force |
| $P$ | internal pressure |
| $R_m$ | radii of curvature at the considered point of the meridian |
| $R_p$ | radii of curvature at the considered point of the parallel |
| $R_n$ | radii of curvature at the considered point of the curve |
| $t_{fp}$ | fiber thickness |
| $E$ | Young modulus |
| $G$ | shear modulus |

### Greek symbols

| | |
|---|---|
| $\Gamma$ | curve inscribed |
| $\theta$ | angle between $Z$ axis and $\vec{OM}$ |
| $\Phi$ | angular position |
| $\alpha$ | winding angle |
| $\lambda$ | coefficient of friction of the fiber |
| $\nu$ | Poisson's ratio |
| $\rho$ | density |
| $\tau$ | shear stress |

## DATA AVAILABILITY STATEMENT

The data that support the findings of this study are available from the corresponding author upon reasonable request.

## ORCID

*Nader Zirak* https://orcid.org/0000-0001-8551-6943

## REFERENCES

1. Balat M. Potential importance of hydrogen as a future solution to environmental and transportation problems. *Int J Hydrogen Energy*. 2008;33:4013-4029.
2. Khouya A. Performance assessment of a dual loop organic rankine cycle powered by a parabolic trough collector for ammonia and hydrogen production purpose. *Int J Ambient Energy*. 2022;43:6149-6166.
3. Li H, Cao X, Liu Y, et al. Safety of hydrogen storage and transportation: an overview on mechanisms, techniques, and challenges. *Energy Rep*. 2022;8:6258-6269.
4. Nicoletti G, Arcuri N, Nicoletti G, Bruno R. A technical and environmental comparison between hydrogen and some fossil fuels. *Energy Convers Manag*. 2015;89:205-213.
5. Lai Q, Sun Y, Wang T, et al. How to design hydrogen storage materials? fundamentals, synthesis, and storage tanks. *Adv Sustain Syst*. 2019;3:1900043.
6. Mohan M, Sharma VK, Kumar EA, Gayathri V. Hydrogen storage in carbon materials—a review. *Energy Storage*. 2019;1:e35.
7. Kalair A, Abas N, Saleem MS, Kalair AR, Khan N. Role of energy storage systems in energy transition from fossil fuels to renewables. *Energy Storage*. 2021;3:e135.
8. Amirante R, Cassone E, Distaso E, Tamburrano P. Overview on recent developments in energy storage: mechanical,

electrochemical and hydrogen technologies. *Energy Convers Manag*. 2017;132:372-387.
9. Groppi D, Astiaso Garcia D, Lo Basso G, Cumo F, De Santoli L. Analysing economic and environmental sustainability related to the use of battery and hydrogen energy storages for increasing the energy independence of small islands. *Energy Convers Manag*. 2018;177:64-76.
10. Baykara SZ. Hydrogen as fuel: a critical technology? *Int J Hydrogen Energy*. 2005;30:545-553.
11. Barreto L, Makihira A, Riahi K. The hydrogen economy in the 21st century: a sustainable development scenario. *Int J Hydrogen Energy*. 2003;28:267-284.
12. Abe JO, Popoola API, Ajenifuja E, Popoola OM. Hydrogen energy, economy and storage: review and recommendation. *Int J Hydrogen Energy*. 2019;44:15072-15086.
13. Ananthachar V, Duffy JJ. Efficiencies of hydrogen storage systems onboard fuel cell vehicles. *Sol Energy*. 2005;78:687-694.
14. Durbin DJ, Malardier-Jugroot C. Review of hydrogen storage techniques for on board vehicle applications. *Int J Hydrogen Energy*. 2013;38:14595-14617.
15. Zhang C, Cao X, Bujlo P, et al. Review on the safety analysis and protection strategies of fast filling hydrogen storage system for fuel cell vehicle application. *J Energy Storage*. 2022;45:103451.
16. Kim S, Han J, Lee S, Jung Y. A study on the mechanical method of observing winding behavior by charging and discharging of type II high pressure hydrogen storage tank. *Trans Korean Hydrog New Energy Soc*. 2022;33:158-163.
17. Kim MS, Ryu JH, Oh SJ, Yang JH, Choi SW. Numerical investigation on influence of gas and turbulence model for type iii hydrogen tank under discharge condition. *Energies MDPI*. 2020;13:6432.
18. Berro Ramirez JP, Halm D, Grandidier JC, Villalonga S, Nony F. 700 bar type IV high pressure hydrogen storage vessel burst - simulation and experimental validation. *Int J Hydrogen Energy*. 2015;40:13183-13192.
19. Koussios S. *Filament Winding: A Unified Approach*. Delft, The Netherlands: Delft University Press; 2002.
20. Bouteloup D. *Éléments de Géométrie Différentielle*. École national de sciences géographiques, 2 édition: Cours de l'ENSG; 2003.
21. Baker EH, Cappelli AP, Kovalevsky L, Rish FL, Verette RM. *Shell analysis manual* (No. NASA-CR-912). NASA; 1968.
22. Flügge W. *Stresses in Shells*. Springer: Berlin/Heidelberg; 1960.
23. Zickel J. Isotensoid pressure vessels. *ARS J*. 1962;32:950-951.
24. Kabir MZ. Finite element analysis of composite pressure vessels with a load sharing metallic liner. *Compos Struct*. 2000;49:247-255.
25. Liang C-C, Chen H-W, Wang C-H. Optimum design of dome contour for filament-wound composite pressure vessels based on a shape factor. *Compos Struct*. 2002;58:469-482.
26. Vasiliev VV, Krikanov AA, Razin AF. New generation of filament-wound composite pressure vessels for commercial applications. *Compos Struct*. 2003;62:449-459.
27. IPST-ULP NB. Cours Matériaux Composites. DESS Mécanique avancée Strat Ind.
28. Newhouse NL, Humphrey WD. Development of the standard test evaluation bottle(STEB). *SAMPE J*. 1986;22:12-15.

**How to cite this article:** Tcharkhtchi A, Villalonga S, Zirak N, Lucas A, Farzaneh S, Shirinbayan M. Optimal dome design for 700 bar hydrogen tank type IV: Hyperelliptic functions and shape factor. *Energy Storage*. 2023;e469. doi:10.1002/est2.469